GSA Data Repository 2018255

What do earthquakes reveal about ambient shear stresses in the upper crust?

(by Guy Simpson)

The Supplementary material provided here includes the following items:

- Description of Mechanical model
- Description of Monte Carlo model
- Table DR1
- Figs. DR1-DR7

Description of Mechanical model

The mechanical model is based on quasi-static force equilibrium and mass balance of a viscoelastic fluid subjected to plane strain deformation and gravity (Simpson, 2015). The model considers a two-dimensional vertical depth section (180 km wide x 60 km deep) containing a single inclined planar fault discontinuity embedded within an elastic material (with a shear modulus of 30×10^9 Pa and Poisson's ratio of 0.25) that is underlain by a high viscosity (10^{19} Pa s) Maxwell viscoelastic material (Fig. DR1). The model faults are assumed to be optimally oriented for frictional sliding. Thus, for a typical background friction coefficient of 0.577, the reverse faults have dips of 30°, whereas the normal faults have dips of 60°. The initial differential stresses in the upper layer are computed assuming that

faults are critically stressed for frictional sliding. The thickness of the faulted upper elastic layer is varied between 5 and 30 km. The lower viscoelastic layer is initially assumed to have zero differential stresses. Models are loaded by imposing constant horizontal velocities (of 50 mm/yr) at the lateral boundaries. The upper boundary is a free surface while all other boundaries are free slip. Solutions to the system of partial differential equations were computed using the continuous Galerkin Finite Element Method using 7-node triangles for velocities and 3 nodes for pressures.

The fault in each model exhibits stick-slip behavior that is governed by rate- and state-friction. Fault friction is calculated from the lab-derived law (Noda et al., 2009)

$$\mu = a \ln\left(\frac{v}{v_o}\right) + \theta \qquad (3)$$

where v is the slip velocity, and θ is a state variable that is computed by solving

$$\frac{\partial \theta}{\partial t} = -\frac{v}{D_c}(\mu - \mu_{ss}) \qquad (4)$$

with the steady state friction value

$$\mu_{ss} = \mu_o + (a - b)\ln\left(\frac{v}{v_o}\right) \qquad (5)$$

Here μ_o is a reference friction coefficient for steady sliding at velocity v_o, a and b are dimensionless parameters characterizing the direct and state evolution effects, respectively, and D_c is the state evolution distance. In this slip-law formulation I set the shear stress on the fault (computed by solving the quasi-static viscoelastic problem) to the fault strength, modified to account for radiation damping, i.e.,

$$\tau = \mu\, \tilde{\sigma}_n + \frac{G}{2c_s} v \qquad (6)$$

where τ and $\tilde{\sigma}_n$ are the shear and effective normal stresses resolved on the fault, G is the shear modulus, c_s is the shear wave speed and μ is the variable friction coefficient given by equation (3). This nonlinear equation (i.e., 6) is solved for the sliding velocity that is then imposed on the fault using the split-node technique (Melosh and Raefsky, 1981).

Although most calculations presented are based on a 'standard' rate- and state-friction law (i.e., equations 3-5) I also carried out simulations incorporating additional dramatic weakening at seismic slip rates, which has been demonstrated in laboratory friction experiments (e.g., Di Toro et al., 2011; Nielsen et al., 2016). Enhanced weakening was introduced (after Noda et al., 2009) by replacing equation (5) with

$$\mu_{LV} = \mu_o + (a - b)\ln\left(\frac{v}{v_o}\right) \qquad (7)$$

and

$$\mu_{ss} = \begin{cases} \mu_{LV} & \text{if} \quad v \le v_w \\ \mu_w + (\mu_{LV} - \mu_w)(v_w/v) & \text{if} \quad v > v_w \end{cases} \qquad (8)$$

Here, μ_{LV} is the conventional low velocity steady-state friction coefficient, *a* and *b* are the standard rate and state parameters, respectively, μ_o is the friction coefficient at the reference sliding velocity v_o, v_w is the sliding velocity at the onset of enhanced weakening and μ_w is the fully weakened friction coefficient (that may be close to 0.2).

Unless stated otherwise, calculations presented here were performed with the following parameter values: μ_o=0.6, v_o =10^{-6} m/s, a = 0.015, c_s=3 km/s, D_c = 0.07 m, $\theta_{initial}$ = 0.5. The state parameter b is taken to be 0.02 until 2 km above the base of the fault when it is assumed to decrease linearly with depth to 0 (Fig. DR1C). This implies that the lower portion of each fault exhibits velocity strengthening behavior (a-b>0) whereas the upper part is velocity weakening (since a-b<0). These parameter values are similar to those used in other earthquake modeling studies. A friction coefficient of 0.6 is chosen to be consistent with Byerlee's law (Byerlee, 1978).

In most simulations presented, elastic waves are neglected but inertial effects are considered via the radiation damping approximation (Rice, 1993), making the

model quasi-dynamic. Additional simulations were performed incorporating full inertia (e.g., see results in Figs. DR2-4). Fluid pressures are not explicitly considered but are incorporated by modifying the initial effective normal stresses. Dynamic effects related coseismic temperature variation are not explicitly treated (e.g., see Noda and Lapusta, 2010) but were investigated indirectly by incorporating enhanced dynamic friction weakening. Off-fault damage is not considered in the simulations, which is considered reasonable since it appears to have a minor influence on earthquake properties such as the total coseismic slip (Thomas et al., 2017).

The model faults exhibit a natural transition from slow slip during the interseismic period to rapid slip during 'earthquakes'. This threshold-type behavior requires adaptive time stepping. The time step is roughly proportional to D_c/v (where D_c is the slip weakening distance and v is the computed slip velocity), so it varies by approximately 10 orders of magnitude between the interseismic and coseismic periods. Calculations performed with excessively large time steps exhibit oscillatory slip velocities (Fig. DR7A) that disappear when the time step is sufficiently reduced (cf. Figs. DR7B and DR7C).

The calculations also require a highly resolved spatial grid in order to achieve accurate and stable solutions. The element size for resolved solutions is controlled by the parameter grouping $2GD_c/\pi\tilde{\sigma}_n(b-\mathrm{a})$ (see Rice 1993). Although

this limit implies exceedingly small elements, I follow a common approach (Rice 1993) by assigning artificially large values to D_c (usually 0.07 m) to relax the element size limit. I also take advantage of an unstructured triangular mesh (Fig. DR1A) that enables relatively small elements (on the order of 100 m long) to be used along the fault whereas the elements elsewhere can be much larger (i.e., by at least one order of magnitude).

Description of Monte Carlo model

The static stress drop of earthquakes in the quasi-dynamic Finite Element models is well described by the empirical relation

$$\Delta\tau = \left(1 - \frac{\mu_d}{\mu_s}\right) \bar{\tau} \qquad (9)$$

where $\Delta\tau$ is the average static stress drop associated with an earthquake, $\bar{\tau}$ is the average shear stress on the fault, μ_d is the kinematic friction coefficient during rupture and $\mu_s$is the static friction coefficient typical of the interseismic period (Fig. DR4). The stress drop is linked to the mean coseismic slip via the well known relation from static crack theory (Scholz, 2002):

$$\bar{u} = \frac{\Delta\tau\, W}{G\, C} \qquad (10)$$

where G is the shear modulus, W is the down-dip rupture width and $C = 4(\lambda + G)/\pi(\lambda + G)$ where λ is the Lamé constant. To evaluate whether one can expect to

observe notable differences in stress drops and slip magnitudes for earthquakes occurring at different depths and in different tectonic stress regimes when the frictional properties also vary, I adopted a Monte Carlo approach , repeatedly solving (9) and (10) for a large number of events (at least 100,000) while randomly varying the tectonic stress regime (i.e., compressive versus extensive), hypocenter depth (which controls the average shear stress), and the static and dynamic friction coefficients within reasonable limits. Faults are assumed to be governed by Andersonian faulting theory. Accordingly, the average vertical stress on the fault is taken as the lithostatic stress at the rupture mid-depth H (i.e., $\rho g H$), while the horizontal stress is that required to initiate frictional sliding, i.e., $\bar{\tau} = \mu_s \tilde{\sigma}_n$ where $\tilde{\sigma}_n$ is the effective normal stress:

$$\tilde{\sigma}_n = \frac{(\sigma_{1+}\sigma_3)}{2} - p_f + \frac{(\sigma_{1-}\sigma_3)}{2}\cos 2\vartheta$$

and $\bar{\tau}$ is the average shear stress on the fault:

$$\bar{\tau} = \frac{(\sigma_{1-}\sigma_3)}{2}\sin 2\vartheta$$

Here σ_1, σ_3, p_f and are the maximum and minimum principal stresses and fluid pressure at H, μ_s is the static friction coefficient and $\tan\vartheta = \mp 1/\mu_s$. For reverse faulting, the vertical and horizontal stresses are assumed to be the minimum and maximum principal stresses, respectively, whereas the converse is true for normal faulting.

Parameters values used for the calculations were chosen to be physically realistic but were fine-tuned by fitting the computed stress drop distribution to natural stress drop data from Allmann and Schearer (2009). Parameters maintained constant were the rock density (ρ =2800 kg m^{-3}), fluid density (ρ_f =1000 kg m^{-3}) and shear modulus (G=30 GPa). The rupture mid-depth (H) was chosen from a normal distribution with a mean of 15 km and a standard deviation of 5 km. The static friction coefficient $\mu_s$was chosen from a normal distribution with a mean of 0.7 and a standard deviation of 0.1. Faults were randomly chosen to be either reverse or normal from a uniform distribution. Good fits with data were obtained, which suggests that the parameters are reasonable, though equally good fits can be obtained with other parameter combinations.

I considered two different end-member fault stress scenarios. In the first (Fig. 3A of main text), fluid pressures were assumed to be hydrostatic, implying that faults operate at relatively high shear stresses. In the second case (Fig. 3B), I assumed that the minimum effective principal stress cannot exceed a constant value $\tilde{\sigma}_c$. The values for $\tilde{\sigma}_c$ were chosen from a Weibull distribution, with scale and shape parameters of 20 MPa and 1.7 MPa, respectively. This implies large fluid overpressures at depth, which leads to low and constant shear stresses below an upper 'normally' pressured regime (Fig. DR7). For both scenarios presented in Figure 3 (main text), the friction drop $\Delta\mu$ (=$\mu_s - \mu_d$) was chosen from a log-

148 normal distribution with means of 0.015 (case 1) and 0.014 (case 2) and standard
149 deviations of 0.0144 (case 1) and 0.012 (case 2).

Table DR1: Rupture properties of large crustal earthquakes (M_w=moment magnitude, L = rupture length, W = down-dip rupture width, D = mean coseismic slip amplitude). Only earthquakes with W≤40 km are studied. Except for the last three entries, the data are from the finite-source rupture model database (SRCMOD; Mai, 2016). The last three earthquake entries are from the following references: Borah Peak (Stein and Barrientos, 1985), Kozani Grevena (Clark et al., 1997), Yutian County (Furuya and Yasuda, 2011). The data are plotted in Fig. 4 (main text).

Location	**Date**	**Depth (km)**	**M_w**	**Rake (°)**	**L (km)**	**W(km)**	**D (m)**
Brawley Swarm	26-Aug-12	6.4	5.45	0	12.75	10.5	0.0782
Sumatra	10-Jan-12	18.37	7.2	173.39	90	21	1.2888
Darfield, South Island, NZ	03-Sep-10	10.84	7.02	153.63	80	26	0.6029
El Mayor-Cucapah, Mexico	04-Apr-10	10	7.35	-174	120	16	1.8905
Haiti	12-Jan-10	12.93	7.1	31.59	50	24	1.3988
Gulf of California	03-Aug-09	9.16	6.9	171.72	108	20.8	0.311
L Aquila, Italy	06-Apr-09	8.64	6.3	-99	30	24	0.1767
Zhongba, Tibet	25-Aug-08	7.63	6.7	306	31	30.49	0.2383
Honshu, Japan	13-Jun-08	9.49	6.8	102.68	42	22	0.8423
Iwate - Miyagi Nairiku	13-Jun-08	6.5	7	99	42.66	17.38	1.8231

Yutian, Tibet	20-Mar-08	4.1	7.1	282.33	53.5	21.99	1.503
Gerze, Tibet	16-Jan-08	4	5.9	273	15	10.02	0.1999
Gerze, Tibet	09-Jan-08	7.5	6.4	293	20	19.58	0.3729
Niigata-ken Chuetsu-Oki	17-Aug-07	8.9	6.6	99	36.75	29.75	0.2882
Noto Hanto, Japan	25-Mar-07	9.62	6.73	138.9	30	16	1.0864
Kuril Islands	13-Jan-07	10	8.1	-97.96	224	40	3.5631
Northern California	15-Jun-05	9	7.2	362.3	102	35	0.6718
Zhongba, Tibet	07-Apr-05	5.98	6.2	292	28	18.67	0.1868
Fukuoka (Japan)	20-Mar-05	14	6.6	-14	26	18	0.6797
Niigata-Ken Chuetsu, Japan	23-Oct-04	10.6	6.62	91.3	28	18	0.6663
Zhongba, Tibet	11-Jul-04	10	6.2	282	20	26.11	0.1357
Miyagi-hokubu (Japan)	25-Jul-03	6.5	6.08	180	12	9.6	0.4736
Carlsberg Ridge	15-Jul-03	11.33	7.6	166.96	320	36	0.5498
Boumerdes (Algeria)	21-May-2003	16	7.25	90	64	32	1.2428
Denali (Alaska)	03-Nov-02	7.5	7.91	228.55	346	30	2.1475
Geiyo (Japan)	24-Mar-01	46.46	6.79	109	30	21	0.8313
Bhuj (India)	26-Jan-01	18	7.66	81	75	35	3.1538
Tottori (Japan)	06-Oct-00	14.5	6.73	180	32	20	0.6157
Kleifarvatn (Iceland)	17-Jun-00	4	5.87	188.04	10	8	0.2811

Duzce (Turkey)	12-Nov-99	18	7.18	182	60	30	1.1204
Hector Mine (Calif.)	16-Oct-99	7.5	7.14	175	54	18	1.8145
Izmit (Turkey)	17-Aug-99	16	7.4	180	93.6	21.6	2.2454
Hida Swarm EV16 (Japan)	18-Sep-98	1.85	4.41	181	3	3.48	0.0134
Iwate (Japan)	03-Sep-98	3	6.3	131	10	10	0.3948
Pumqu-Xainza, Tibet	25-Aug-98	8.25	6.16	300.66	38	23	0.0679
Antarctica Strike-Slip Segment	25-Mar-98	12	7.98	1	305	35	2.9824
Colfiorito Sequence # 3 (Italy)	14-Oct-97	5.58	5.86	270	9	6	0.4512
Colfiorito Sequence # 1 (Italy)	26-Sep-97	4.04	5.72	270	7.5	7.5	0.2744
Colfiorito Sequence # 2 (Italy)	26-Sep-97	5.1	5.97	270	12.5	7.5	0.396
Yamaguchi (Japan)	25-Jun-97	8.2	5.82	180	16	14	0.0812
Kagoshimaen-hoku-seibu (Japan)	26-Mar-97	7.6	6.1	0	15	10	0.3391
Hyuga-nada2 (Japan)	02-Dec-96	20.4	6.68	80	29.2	29.2	0.4218
Hyuga-nada1 (Japan)	19-Oct-96	11.6	6.81	80	32.12	32.12	0.5415
Pumqu-Xainza, Tibet	03-Jul-96	8.25	6.08	301.42	25	18	0.1022
Kobe (Japan)	17-Jan-95	14.3	6.9	180	60	20	0.6532
Northridge (Calif.)	17-Jan-94	17.5	6.66	105	23	27	0.5213
Pumqu-Xainza, Tibet	20-Mar-93	8.25	6.29	294.33	30	22	0.1393
Landers (Calif.)	28-Jun-92	7	7.2	180	77	15	1.8878

Joshua Tree (Calif.)	23-Apr-92	12.5	6.15	0	22	20	0.1245
Ungava (Canada)	25-Dec-89	2.5	6.02	90	13	6	0.4636
Loma Prieta (Calif.)	18-Oct-89	17.6	6.98	145	40	14	1.8038
Superstition Hills (Calif.)	24-Nov-87	10	6.51	180	20	11.5	0.8291
Elmore Ranch (Calif.)	24-Nov-87	10	6.52	0	25	10	0.8976
Whittier Narrows (Calif.)	01-Oct-87	14.6	5.89	90	10	10	0.2625
Nahanni2 (Canada)	23-Dec-85	8	6.66	90	48	21.24	0.4844
Nahanni1 (Canada)	05-Oct-85	8	6.66	90	40	17.4	0.5359
Nagano-ken seibu (Japan)	14-Sep-84	3	6.29	0	12	9	1.0083
Morgan Hill (Calif.)	24-Apr-84	8.5	6.28	180	30	10	0.2644
Borah Peak (Idaho)	28-Oct-83	16	6.82	280	52	26.64	0.357
Izu-hanto-toho-oki (Japan)	29-Jun-80	8	6.61	0	20	12	1.06
Imperial Valley (Calif.)	15-Oct-79	8	6.35	180	42	10	0.4118
Coyote Lake (Calif.)	06-Aug-79	8	5.92	176	10	10	0.2608
Izu-hanto-oki (Japan)	09-May-74	8	6.56	180	25	9	1.06
San Fernando (Calif.)	09-Feb-71	13	6.82	83	18	20	1.6006
Gifu-ken-chubu (Japan)	09-Sep-69	2	6.43	180	20	11.2	0.68
Kitamino (Japan)	19-Aug-61	10	6.47	90	16	12	0.9083
Fukui (Japan)	28-Jun-48	10.14	6.65	351	60	18	0.3

	Borah Peak	28-Oct-83	16	6.9	-90	18	2
	KozaniGrevena	13-May-95	ca. 15	6.5	-90	20	0.3
	Yutian County, Xinjiang	20-Mar-08	ca. 15	7.1	-90	24	1

158

159

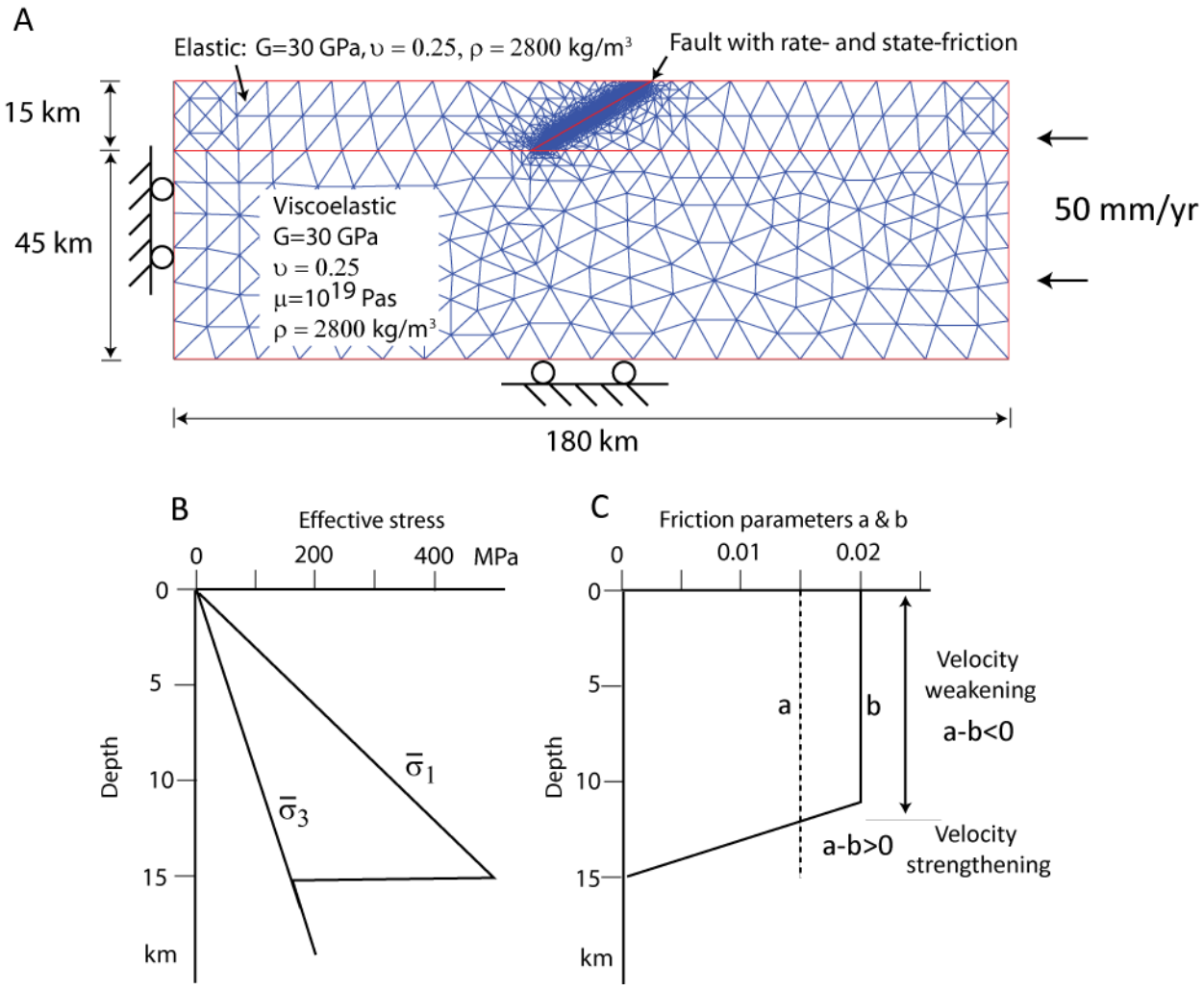

Figure DR1 A-C: Typical mode setup for earthquake simulation on a reverse fault. A: Planar reverse fault embedded in an elastic layer that overlies a viscoelastic layer, subjected to remote loading and gravity. Triangles are finite elements on which the solution is computed. B: Initial effective stress state versus depth in the upper part of the model. C: Variation of the rate- and state-friction parameters *a* and *b* on the fault.

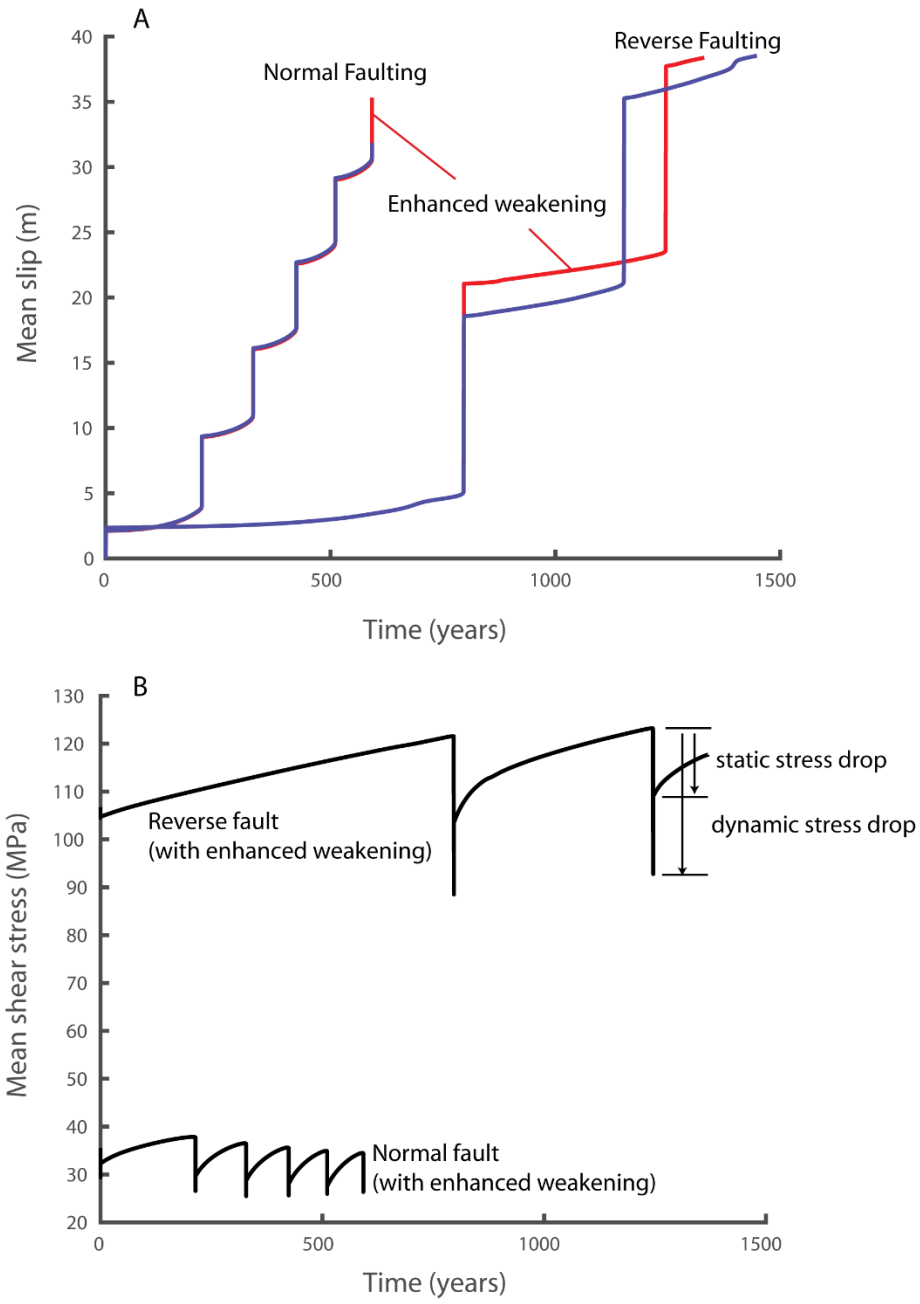

168

169 **Figure DR2 A-B:** Mean slip versus time (A) and mean shear stress versus time (B) on reverse

170 and normal faults in numerical experiments incorporating full inertia, with and without enhanced

171 dynamic weakening (μ_w =0.2, v_w = 0.1 m/s, see equation 8 above). The average slip rate on the

172 normal fault is greater than on the reverse fault because the former has a larger dip.

173

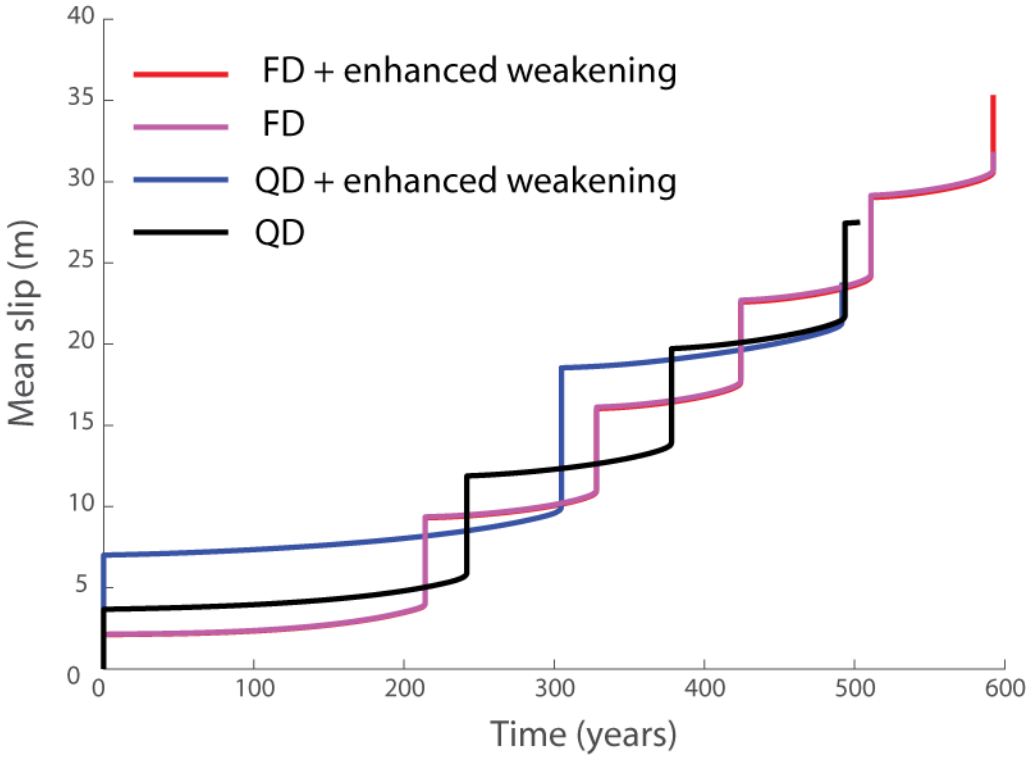

Figure DR3: Computed mean slip versus time on a normal fault with and without enhanced dynamic weakening and full inertia (FD = fully dynamic, QD = quasi-dynamic). Simulations with enhanced weakening were calculated with μ_w =0.2, v_w = 0.1 m/s (see equation 8 above). Otherwise, classic rate-and state-dependent friction was assumed, using the parameters listed above.

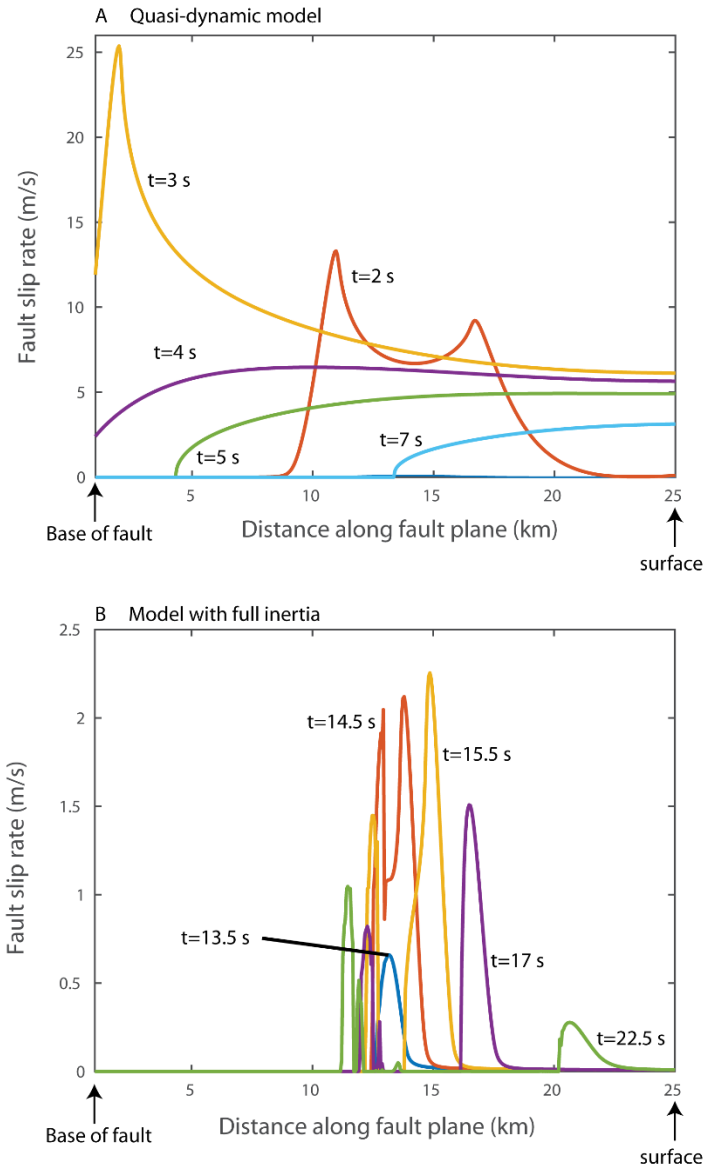

Figure DR4 A-B: Comparison of the slip rate versus distance along the fault for simulations using the quasi-dynamic approximation (A) and full inertia (B). In both cases, the ruptures are on reverse faults with identical material properties. The rupture in the quasi-dynamic simulation propagates as a crack, while that in the simulation with full inertia propagates as a slip pulse. Even so, the simulations exhibiting pulse-like behavior still show larger slips on reverse faults than normal faults, when ambient stress levels are high (see Fig DR2).

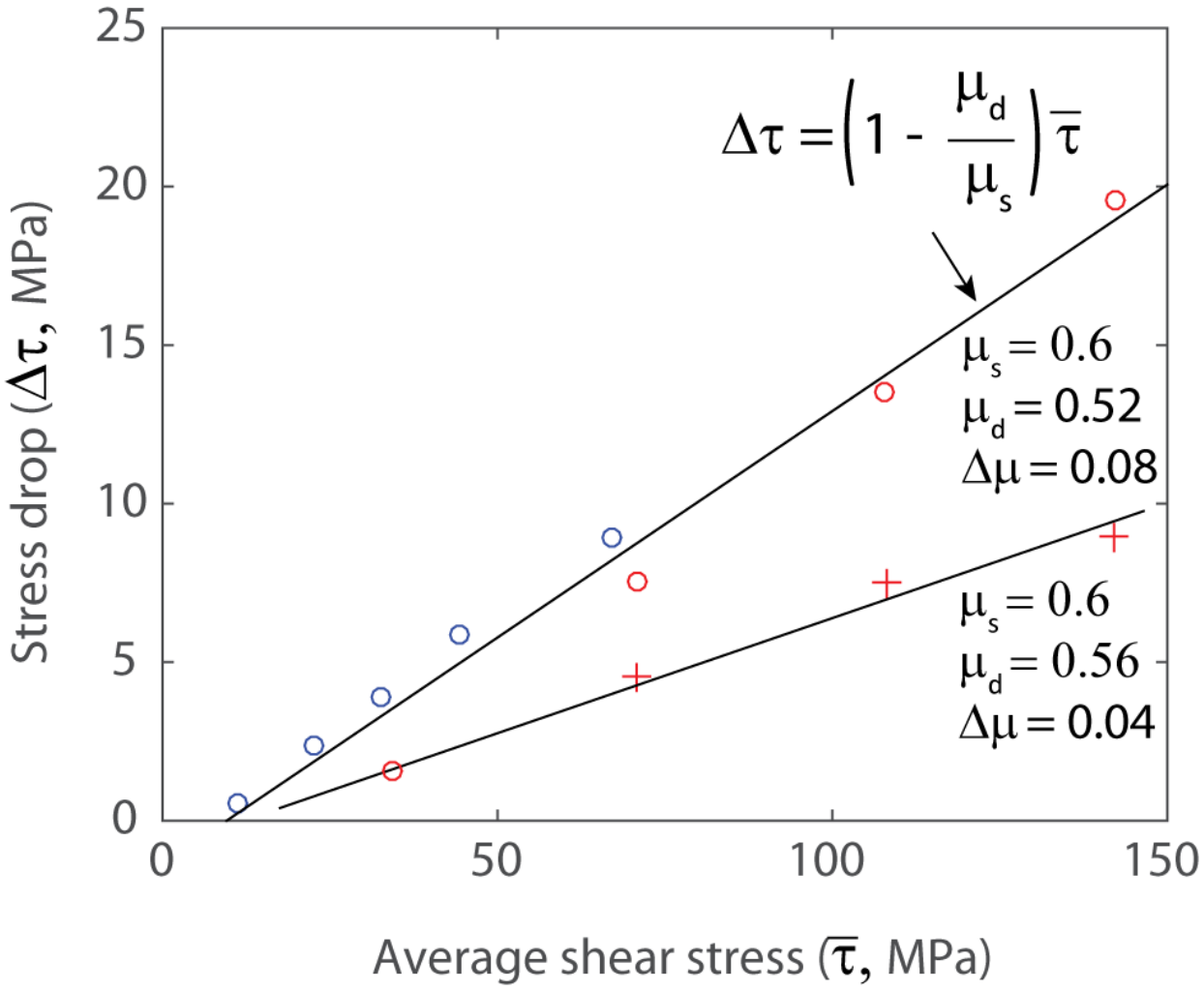

Figure DR5: Scaling between static stress drop versus average shear stress. Symbols show results of the finite element quasi-dynamic simulations while the solid lines show stress drop predictions based on equation (9).

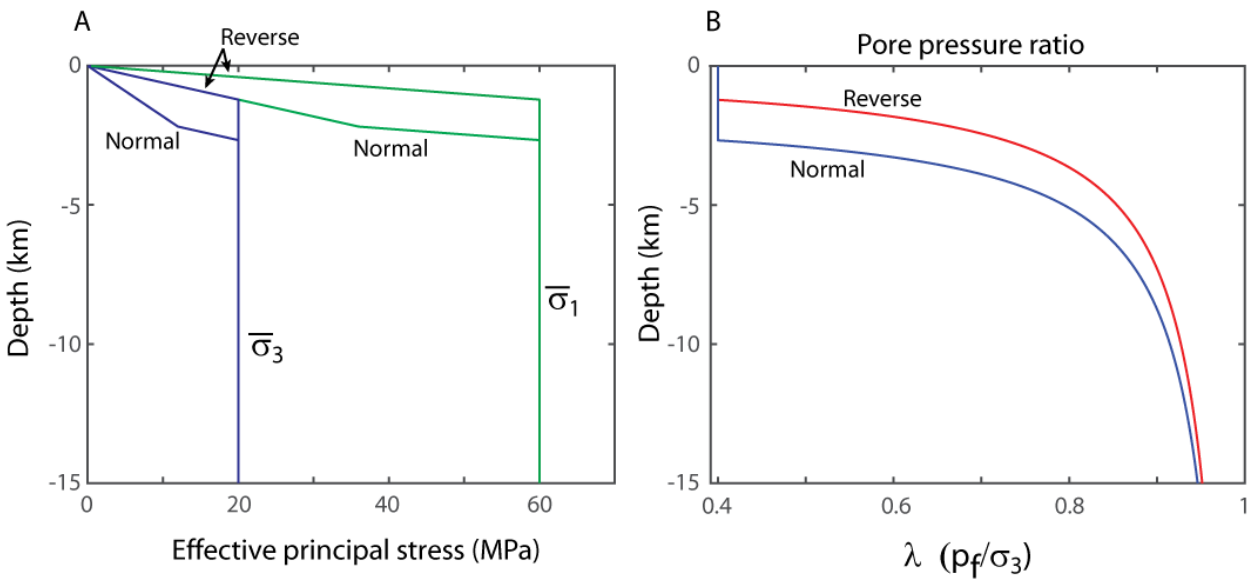

Figure DR6 A-B: Illustration of initial effective principal stress state in models considering fluid overpressures. The upper part of the crust is assumed to have hydrostatic fluid pressures whereas the underlying rocks have overpressures governed by the condition $\tilde{\sigma}_3 = \tilde{\sigma}_c$ where $\tilde{\sigma}_c$ is a constant (in this case 20 MPa). Stresses are defined by Andersonian faulting theory with a friction coefficient of 0.6 and a rock density of 2800 kg/m^3. A: Variation of the effective principal stresses with depth for reverse and normal faulting stress regimes. B: Variation in the pore pressure ratio (defined here as the ratio between the fluid pressure and the total minimum principal stress) with depth for reverse and normal fault regimes.

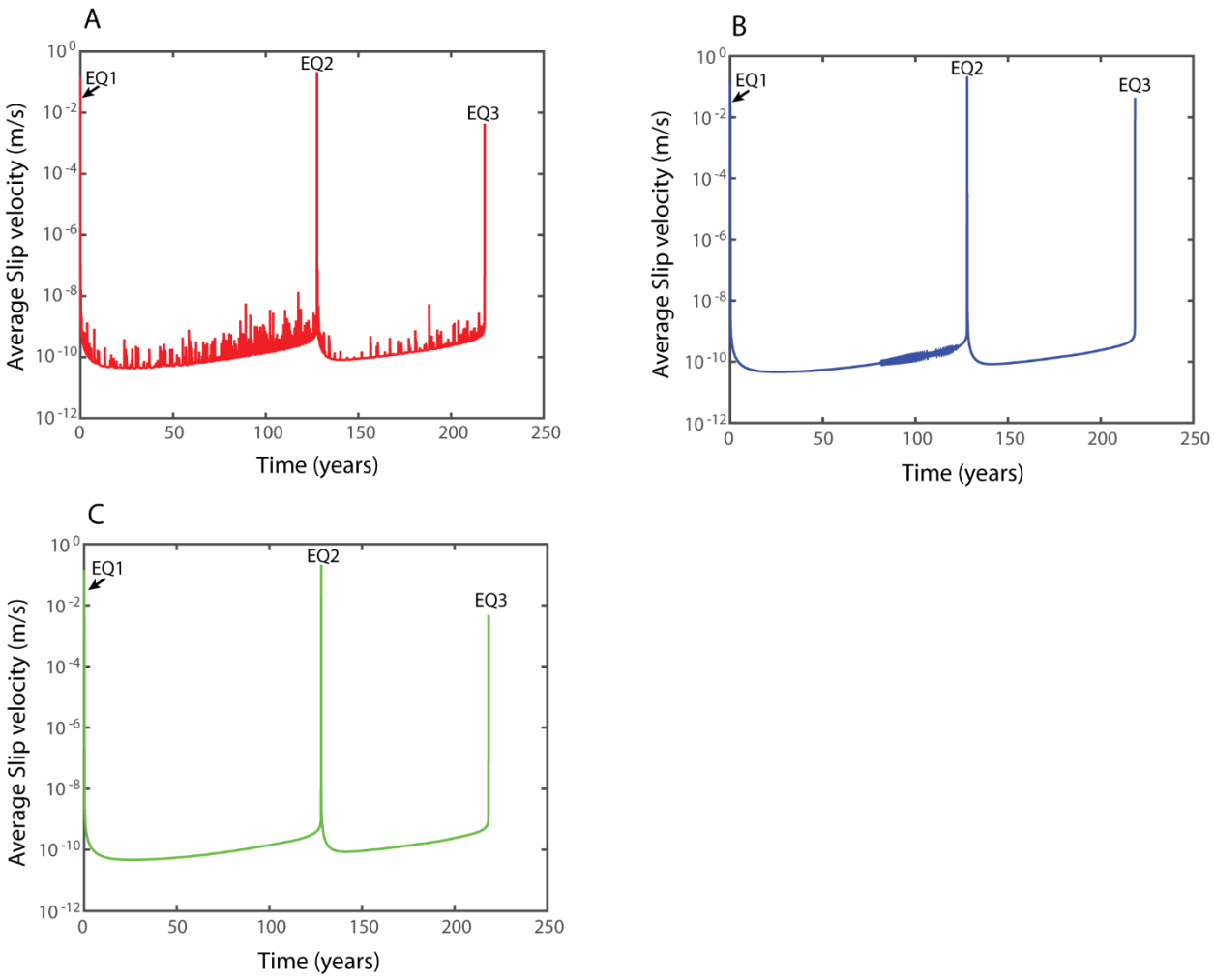

206

207 **Figure DR7 A-C:** Illustration of time scale resolution in quasi-dynamic numerical experiments.

208 Plots show the mean slip velocity on the fault versus time for quasi-dynamic simulations

209 performed with different temporal resolutions. The excessively large time step in (A) leads to

210 numerical oscillations. Reducing the time step by a factor of two reduces the oscillations (B),

211 which disappear entirely when the time step is decreased another two times (C).

212

References

Allmann, B.P. and Shearer, P.M., 2009, Global variations of stress drop for moderate to large earthquakes: Journal of Geophysical Research, v. 114, doi:10.1029/2008jb005821.

Byerlee, J.D. Friction of rocks, Pure and Applied Geophysics, v. 116, 615-626.

Clarke, P. J., Paradissis, D., Briole, P., England, P.C., Parsons, B.E., Billiris, H., Veis, G., Ruegg, J.-C., 1997, Geodetic investigation of the 13 May 1995 Kozani-Grevena (Greece) Earthquake: Geophysical Research Letters, v. 24, p. 707-710, doi:10.1029/97GL00430.

Di Toro, G., Han R., Hirose, T., De Paola, N., Nielsen, S., Mizoguchi, K., Ferri, F., Cocco, M., Shimamoto, T., 2011, Fault lubrication during earthquakes: Nature, v. 471, p. 494-498, doi:10.1038/nature09838.

Furuya, M. and Yasuda, T., 2011, The 2008 Yutian normal faulting earthquake (Mw 7.1), NW Tibet: Non-planar fault modeling and implications for the Karakax Fault: Tectonophysics, v. 511, p. 125-133, doi:10.1016/j.tecto.2011.09.003.

Mai, M., 2016, Finite-Source Rupture Model Database, <http://equake-rc.info/SRCMOD/>.

Melosh, H.,J. and Raefsky, A, 1981, A simple and efficient method for introducing faults into finite element computations: Bulletin of the Seismological Society of America, v. 71, p. 1391-1400.

Nielsen, S., Spagnuolo, E., Smith, S.A.F., Violay, M., Di Toro, G., and A. Bistacchi, 2016, Scaling in natural and laboratory earthquakes: Geophysical Research Letters, v. 43, 1504-1510, doi: 10.1002/2015GL067490.

Noda, H., Dunham, E.M. and Rice, J.R., 2009, Earthquake ruptures with thermal weakening and the operation: Journal of Geophysical Research, v. 114, B07302, doi:10.1029/2008JB006143.

Noda, H., and Lapusta, N., 2010, Three-dimensional earthquake sequence simulations with evolving temperature and pore pressure due to shear heating: effect of heterogeneous hydraulic diffusivity: Journal of Geophysical Research, v. 115, doi:10.1029/2010JB007780.

Rice, J. R., 1993, Spatio-temporal complexity of slip on a fault: Journal of Geophysical Research, v. 98, p. 9885–9907, doi:10.1029/93JB00191.

Scholz, C.H., 2002, The mechanics of earthquakes and faulting. Cambridge University Press, Cambridge, 471 p.

Simpson, G.D. H., 2015, Accumulation of permanent deformation during earthquake cycles on reverse faults: Journal of Geophysical Research, v. 120, p. 1958-1974, doi:10.1002/2014JB011442.

Stein, R.S. and Barrientos, S.E., 1985, Planar High-Angle faulting in the Basin and Range: Geodetic analysis of the 1983 Borah peak, Idaho, Earthquake: Journal of Geophysical Research, v. 90, p. 11355-11366.

Thomas, M.Y., Bhat, H.S. and Klinger, Y, 2017, Effect of brittle off-fault damage on earthquake rupture dynamics. In: Fault zone dynamic processes: evolution of fault zone dynamic processes: Evolution of fault properties during seismic rupture. Edited by Thomas, M., Mitchell, T and Bhat H. Geophysical Monograph, 227, p. 255-280.

256

257